Published in final edited form as:
Neuroscience. 2011 March 17; 177: 183–194. doi:10.1016/j.neuroscience.2011.01.015.

THE DYT1 CARRIER STATE INCREASES ENERGY DEMAND IN THE OLIVOCEREBELLAR NETWORK

Yu Zhao[a], **Nutan Sharma**[b], and **Mark S. LeDoux**[a]

[a]Departments of Neurology and Anatomy & Neurobiology, University of Tennessee Health Science Center, Memphis, Tennessee, USA

[b]Department of Neurology, Massachusetts General Hospital and Harvard Medical School, Boston, Massachusetts, USA

Abstract

DYT1 dystonia is caused by a GAG deletion in *TOR1A*, the gene which encodes torsinA. Gene expression studies in rodents and functional imaging studies in humans suggest that DYT1 dystonia may be a network disorder of neurodevelopmental origin. To generate high resolution metabolic maps of DYT1 dystonia and pinpoint dysregulated network elements, we performed 2-deoxyglucose autoradiography and cytochrome oxidase (CO) histochemistry in transgenic mice expressing human mutant (hMT1) torsinA and wild-type littermates. In comparison with controls, hMT1 mice showed increased glucose utilization (GU) in the inferior olive (IO) medial nucleus (IOM), IO dorsal accessory nucleus and substantia nigra compacta, and decreased GU in the medial globus pallidus (MGP) and lateral globus pallidus. The hMT1 mice showed increased CO activity in the IOM and Purkinje cell layer of cerebellar cortex, and decreased CO activity in the caudal caudate-putamen, substantia nigra reticulata and MGP. These findings suggest that (1) the DYT1 carrier state increases energy demand in the olivocerebellar network and (2) the IO may be a pivotal node for abnormal basal ganglia-cerebellar interactions in dystonia.

Keywords

dystonia; globus pallidus; glucose utilization; cytochrome oxidase histochemistry; inferior olive; Purkinje cells

Dystonia is characterized by sustained and involuntary muscle contractions resulting in twisting and repetitive movements or abnormal postures (Fahn, 1988). Early-onset primary dystonia typically begins in the distal portions of a limb and often spreads to involve other regions of the body. A common genetic cause of early-onset primary dystonia is a heterozygous GAG deletion in the *TOR1A* gene (i.e., DYT1 dystonia) which results in the loss of a single glutamic acid residue near the C-terminus of the encoded protein torsinA (Ozelius et al., 1997). DYT1 dystonia is transmitted in an autosomal dominant fashion with reduced penetrance. Symptoms usually become manifest in childhood. Onset before the age

Address correspondence to: Mark S. LeDoux, M.D., Ph.D., University of Tennessee Health Science Center, Department of Neurology, 855 Monroe Avenue, Link Building, Suite 415, Memphis, Tennessee 38163, Phone: 901-448-1662, FAX: 901-448-7440, mledoux@uthsc.edu.

of 4 or after the age of 28 is uncommon (Bressman et al., 1998; Bressman et al., 2000; Xiao et al., 2009).

Using [18F]-fluorodeoxyglucose and positron emission tomography (PET) in humans, both manifesting and non-manifesting carriers of the DYT1 mutation have shown similar patterns of hypermetabolism when compared to neurologically-normal controls (Eidelberg, 1998). In movement-free conditions, both manifesting and non-manifesting DYT1 carriers showed increased metabolic activity in the lentiform nuclei, cerebellum and supplementary motor areas. In movement-related conditions, only manifesting DYT1 carriers showed increased metabolic activity in the midbrain, cerebellum and thalamus. More recently, magnetic resonance diffusion tensor imaging has demonstrated reduced integrity of cerebellothalamocortical fiber tracts in both manifesting and non-manifesting carriers of the DYT1 ΔGAG mutation (Argyelan et al., 2009). The nigrostriatal pathway has also been implicated in the network pathophysiology of DYT1 dystonia. PET studies have shown that non-manifesting carriers exhibit reduced dopamine D2 receptor binding (Asanuma et al., 2005). In addition, post-mortem neurochemical studies have noted a significant increase in dopamine turnover (Augood et al., 2002). Taken together, these findings suggest that DYT1 dystonia is a circuit disorder of the nervous system.

Mice that overexpress mutant human torsinA (hMT1) show abnormalities in nigrostriatal neurochemistry, similar to what has been found in humans with DYT1 dystonia. Zhao et al (2008) detected increased striatal DOPAC and HVA levels in hMT1 mice consistent with increased dopamine turnover. In addition, hMT1 mice display attenuated amphetamine-induced dopamine release, altered activity of the dopamine transporter, and abnormal dopaminergic D2 receptor responses in striatal cholinergic interneurons (Pisani et al., 2006; Balcioglu et al., 2007; Sciamanna et al., 2009; Hewett et al., 2010). Thus, the physiological and neurochemical abnormalities found in humans with DYT1 dystonia can be exposed with greater clarity in animal models of this order.

Metabolic mapping in animal models has provided critical insights into the network pathophysiology of a variety of movement and neurodegenerative disorders (Kimura et al., 1980; Brown and Lorden, 1989; Mitchell et al., 1992; Vila et al., 1996; Nobrega et al., 1998; Richter et al., 1998). Functional neuroimaging in humans suffers from limited spatial resolution and may be confounded by the effects of genetic background, age and gender. To reduce these effects and generate data of higher spatial resolution, 2-deoxy-D-glucose (2-DG) autoradiography and cytochrome oxidase (CO) histochemistry were performed in transgenic mice expressing either human wild-type (hWT) or mutant (hMT1) torsinA and wild-type (WT) littermates. The combined use of CO histochemistry and 2-DG autoradiography provides complementary information regarding metabolic activity in specific cell groups and local circuits (Jacquin et al., 1993).

EXPERIMENTAL PROCEDURES

Animals

Adult male mice, between 3 to 4 months of age, that over express human mutant torsinA (hMT1; N = 9), human wild type torsinA (hWT; N = 8) and their non-transgenic littermates (WT; N = 9) were used for quantitative analyses of brain metabolism using 2-DG autoradiography and CO histochemistry. CO histochemistry reflects oxidative energy metabolism of neural tissues, especially neurons and is thought to provide information reflecting long-term neuronal metabolic demand over days or weeks (Di Rocco et al., 1989; Wong-Riley, 1989; Gonzalez-Lima and Garrosa, 1991; Hevner et al., 1995). In contrast, the glucose analogue, 2-DG, is taken up by glucose transporters in neurons and glia but cannot undergo glycolysis. Thus, 2-DG reveals the instantaneous glucose demand of neural and

extra-neural tissues and 2-DG autoradiography is thought to reflect short-term metabolic demands (Wree and Schleicher, 1988; Wree, 1990; Duncan and Stumpf, 1991; McCasland and Graczyk, 2001). Mice were maintained in a temperature-controlled environment with free access to food and water. Light was controlled on a 12 hr light/dark cycle. All procedures were approved by the University of Tennessee Health Science Center Animal Care and Use Committee and performed in accordance with the National Institutes of Health Guide for the Care and Use of Laboratory Animals.

Tissue preparation

The protocol for combined 2-DG autoradiography and CO histochemistry was adapted from McCasland and Graczyk (2001). After a single dose of 2-DG (0.165 μCi/g) given by intraperitoneal injection, mice were placed in individual cages for 45 min, overdosed with pentobarbital and rapidly perfused (< 2 min) with heparinized saline followed by a mixture of 2.5% paraformaldehyde/1.5% glutaraldehyde/4% sucrose in 0.1 M phosphate buffer (PB). Of note, perfusion-fixation with paraformaldehyde and/or glutaraldehyde for 2-DG autoradiography has been employed by numerous investigators as a means of preserving tissue integrity for CO histochemistry and immunocytochemistry (Silverman and Tootell, 1987; McCasland and Woolsey, 1988; Redies and Gjedde, 1989). Brains were rapidly removed, blocked, frozen in pre-chilled isopentane at −40 °C and stored at −80 °C. Twenty μm coronal tissue sections were prepared using a Leica CM3050 S cryostat (Leica Microsystems Inc., Bannockburn, IL, USA) and collected in 5 rostral-caudal coronal series onto SuperFrost®-Plus glass slides (Fisher Scientific, Pittsburgh, PA, USA). One series of sections was air-dried overnight and stained with cresyl violet (Sigma-Aldrich, St. Louis, MO, USA). The remaining 4 series of sections were stored at −80 °C in vacuum-sealed slide containers until further processing for 2-DG autoradiography imaging and CO histochemistry.

Regions of interest (ROIs)

The nomenclature and abbreviations used for GU and CO ROIs (Tables 1 and 2) were adapted from Franklin and Paxinos (1997). In general, CO histochemistry (tissue sections, Fig. 1) generated data of higher spatial resolution than 2-DG autoradiography (film, Fig. 2). For example, CO activity was well delineated among the layers of cerebellar cortex (molecular, Purkinje and granule cell) and regions of hippocampus. Accordingly, a larger number of ROIs were interrogated for CO activity than GU. Mean values for optical density (O.D.) were derived from four to six sections covering the rostal-caudal extent of each ROI. To generate O.D. values for the layers of cerebellar cortex, measurements were made from the vermis (N = 6) and hemispheres (N = 6).

Image acquisition and analysis of GU

Brain sections were exposed to Kodak Biomax MR Film together with ^{14}C Microscale™ autoradiography standards (RPA504, Amersham Biosciences, Piscataway, NJ, USA) for 7 days. Due to technical issues, data from 4 mice (1 hMT1, 2 hWT, and 1 WT) was not suitable for subsequent analyses of GU. Autoradiographic images were acquired in transmission mode (ScanMaker 9800 XL, Microtek, Carson, CA, USA) and imported into ImageJ (Java version of NIH Image, http://rsb.info.nih.gov/ij/) for neuroanatomical ROI quantification of radioactivity. The investigator performing ROI analyses was blinded to genotype. O.D. was calibrated to the set of autoradiography standards to generate measures of radioactivity (nCi/g tissue) for each ROI. Due to potential confounding variables such as peritoneal absorption and global differences in GU, ROI GU data from each mouse was converted to Z-scores.

CO histochemistry

CO histochemistry was performed using a protocol modified from that of Gonzalez-Lima and Jones (1994). The reaction solution was freshly made in 0.1 M PB (pH. 7.4) and contained 0.06% diaminobenzidine, 0.02% cytochrome c and 4.5% sucrose. Brain sections and standards of brain homogenate were incubated in the reaction solution for 1.5 h in the dark at 37 °C in a shaking water bath. The reaction was stopped by washing the slides with 0.1M PB/4% sucrose for 5 min × 3. After dehydration in ascending concentrations of ethanol (30%, 50%, 75%, 95%, and 100%), the slides were cleared with xylene and coversliped with Permount (Fisher Scientific, Pittsburgh, PA).

Fresh whole brains from 5 wild-type C57BL/6 mice (littermates) were completely homogenized on ice with a manual Dounce-glass homogenizer. The homogenates were transferred to 2 ml microcentrifuge tubes. After centrifugation at 1000 rpm (4 °C) for 2 min, the tubes were fast frozen in isopentane (−40 °C) and stored at −80 °C. Brain homogenates were sectioned on a cryostat at a series of thicknesses covering the entire range of CO activity (5 μm, 10 μm, 20 μm, 30 μm, 40 μm, 50 μm and 60 μm), collected onto SuperFrost®-Plus glass slides and stored at −80 °C in a vacuum-sealed slide container for use as CO activity standards.

The CO activity of the brain homogenates was determined with a spectrophotometric method as modified from Hess and Pope (1953) by Gonzalez-Lima and Jones (1994). Briefly, the sample solution was made by mixing the brain homogenate in 0.75% deoxycholate at a ratio of 0.01 g/5 ml. Then, 0.1 ml of the sample solution was added to 0.9 ml of a 30 μM reduced cytochrome c solution in a 10 mm cuvette and mixed well. The O.D. was read with a SmartSpec3000 spectrophotometer (Bio-Rad Laboratories, Hercules, CA, USA) at 550 nm using the kinetic program with readings taken at 15 s intervals over 3 minutes. The change in spectrophotometric reading (ΔO.D.) was used in the calculation of CO activity with an extinction coefficient of 19000/M-cm. Each sample solution was read in triplicate and each homogenate underwent the reaction 5 times. A mean activity of 30.02 mmol/min-g of tissue was used for densitometric analysis.

Brain slides were scanned using Polaroid SprintScan 4000 (Polaroid Corporation, Waltham, MA, USA) with PathScan Enabler (Meyer Instrument, Houston, TX, USA) at a resolution of 2000 dpi along with the brain homogenate standards. Digital images were imported into ImageJ for quantitative densitometry analysis and the standards were used to convert O.D. levels into enzyme activity values reported as μmol/min-g of tissue for each ROI. Due to potential confounding variables such as global differences in CO activity, ROI data from each mouse was converted to Z-scores.

Statistics

All statistical analyses were performed with SAS®. In previous work, we showed that hWT mice expressed very low levels of wild-type torsinA transcript (Zhao et al., 2008). Compatible with those results, GU and CO activity within ROIs from hWT and WT mice were found to be highly correlated in the experiments described herein (GU mean $r = 0.968$, CO activity mean $r = 0.952$, Fig. 3). In addition, two-sided unpaired t-tests were used to evaluate differences in mean GU and CO ROI Z-scores between WT and hWT mice. Even without correction for multiple comparisons, no GU ROI Z-score showed a significant difference between WT and hWT mice ($P > 0.01$, for all). Among the 56 CO ROIs, only the ventral pallidum (VP) differed between WT and hWT mice ($P < 0.01$). Accordingly, data from hWT and WT mice were pooled for comparisons with hMT1 mice in order to increase statistical power. Statistical analyses for mean GU and CO values between hMT1 and control mice were assessed using two-sided unpaired t-tests. The level of significance (α)

was set at 0.01, and, given the large number of ROIs, no corrections were made for multiple comparisons. We also examined Pearson correlations of GU and CO activity as described by Brown and Lorden (1989). Pairs of ROIs were chosen *a priori* based on known patterns of anatomically connectivity. Our analyses were limited to basal ganglia and olivocerebellar pathways.

Principal component analysis (PCA) was applied to GU and CO ROI Z-scores as a variable reduction method and to expose coherent subsets of anatomical regions associated with the DYT carrier state (i.e., hMT1 mice). The principal axis method was use to extract components. Varimax rotation was used, which results in orthogonal components. Five components were retained for each analysis based, in part, on scree tests, proportion of variance accounted for and interpretability. Variables with loadings >0.5 restricted to single components were retained in order to generate component scores. Component scores were calculated for each animal and used for statistical comparisons of hMT1 and control mice with two-sided t-tests subjected to Bonferroni correction. Below is the general formula for calculation of component scores:

$$C_N = a_{N1}(X_1) + a_{N2}(X_2) + a_{N3}(X_3) + a_{N4}(X_4) + a_{N5}(X_5)$$

where c_1 = mouse's score on principal component N,

$a_{N1} \ldots a_{N5}$ = loadings for ROIs 1 – 5

$X_1 \ldots X_5$ = Z-scores for ROIs 1 –5

RESULTS

GU

Based on mean GU across all 40 neuroanatomical ROIs, there were no differences in whole brain GU between hMT1 and control mice. However, a comparison of ROI GU Z-scores in discrete brain regions between hMT1 and control mice identified several ROIs with altered acute metabolic activity in the mutants (Table 1). Of note, of the 10 regions showing Z-score *P* values less than 0.01, 9 were located in the basal ganglia (medial globus pallidus [MGP}, substantia nigra compacta [SNC], lateral globus pallidus [LGP] and subthalamic nucleus [STh]), olivocerebellar structures (IO medial nucleus [IOM], IO dorsal accessory nucleus [IOD] and lateral cerebellar nucleus [Lat]), or their immediate efferent nuclei (ventromedial thalamic nucleus [VM] and red nucleus magnocellular [RMC]). In comparison with control mice, hMT1 mice showed significantly increased GU in the IOM ($P = 0.0017$), IOD ($P = 0.0049$) and SNC ($P = 0.0064$). Trends towards higher GU were also noted in hMT1 cerebellar cortex (hemisphere [CHem] and vermis [CVer]), Lat, RMC, STh and VM. In comparison with control mice, hMT1 mice had decreased GU in the MGP ($P = 0.0009$) and LGP ($P = 0.0098$).

CO activity

The regional distribution of CO staining in control mouse brain was similar to that found in rats (Hevner et al., 1995). The highest levels of CO histochemical staining were found in the cerebellar cortex, cerebellar nuclei, red nucleus, caudate-putamen, STh and subregions of the cerebral cortex. The lowest levels of CO histochemical staining were found in the corpus callosum and globus pallidus. CO staining in the gray matter was not dependent on the density of cell bodies. For example, in the SNC and granule cell layer of the dentate gyrus, two regions with high cell packing densities, CO staining was not particularly intense. However, in some regions with a relative paucity of cell bodies, such as the molecular layer of the cerebellar cortex and the stratum lacunosum-moleculare in the hippocampus, relatively high CO staining was visible. Similar variability in the intensity of staining was

seen between cell bodies and neuropil in different brain regions. For example, the cell bodies of neurons in red nucleus and vestibular nuclei had the most intense CO staining, whereas, in the caudate-putamen and deep cerebellar nuclei, both the cell bodies and the neuropil stained equally well.

Densitometric analysis of CO activity encompassing all 56 neuroanatomical ROIs did not reveal any difference in whole brain CO activity between hMT1 and control mice. However, comparisons of Z-scores did reveal significant differences in CO activity within individual ROIs between hMT1 mice and controls. As seen in Table 2, there were significant increases in CO activity in the IOM ($P = 0.0059$) and Purkinje cell layer of the cerebellar cortex ($P = 0.0074$) in hMT1 mice in comparison with controls. In addition, all three cerebellar nuclei included in ROI analyses (Lat, anterior interposed nucleus [AInt] and medial cerebellar nucleus [Med]) tended to show higher CO activity in hMT1 mice ($P < 0.1$, for all). In contrast, all three subdivisions of the caudate-putamen included in our analyses (caudal [CPuC], rostral-ventral [CPuRV] and rostral-dorsal [CPuRD]) tended to show lower CO activity in hMT1 mice in comparison with controls ($P < 0.01$). When compared to controls, significant decreases in hMT1 CO activity were found in CPuC ($P = 0.0008$), substantia nigra reticulata (SNR, $P = 0.0025$) and MGP ($P = 0.0097$).

Correlation analysis

For additional interrogation of functional relationships within regions of the basal ganglia, cerebellum, and their input and output nuclei, correlation coefficients between ROIs were analyzed with GU and CO histochemistry (Table 3). The projection from AInt and Lat to RMC was altered in hMT1 mice. First, the positive correlation between CO activity in the cerebellar nuclei (AInt and Lat) and RMC noted in control mice was absent in hMT1 mice. Second, correlations in GU between the cerebellar nuclei and RMC were stronger in the hMT1 mice than in controls. The projection from Lat to the thalamus (ventrolateral [VL] and VM) was also abnormal; GU correlations were positive in controls whereas they were negative in hMT1 mice. As additional evidence of olivocerebellar dysfunction, correlations of CO activity between inferior olivary subnuclei (IOM and IOD) and their efferent cerebellar nuclei (Med and AInt) were positive in controls but negative in hMT1 mice.

Striatopallidal and subthalamic-pallidal interactions showed evidence of derangement in hMT1 mice. To begin with, CO activity correlations between the rostal caudate-putamen (CPu) and both the MGP and LGP were weaker in hMT1 than in controls. However, these correlations were maintained in the caudal caudate-putamen. Secondly, all GU correlations between the CPu and globus pallidus were positive in controls but negative in hMT1 mice. Lastly, the STh-MGP and -LGP CO activity correlations were negative in controls but positive in hMT1 mice.

GU and CO PCA

Examination of Table 4 shows that the extracted components showed marked anatomical loading differences between hMT1 and control mice. In control mice, those ROIs contributing to individual components tended to be concentrated in contiguous brain regions. For instance, secondary motor cortex, secondary somatosensory cortex, somatosensory 1 barrel field and cingulum load on the first GU component in controls. Similarly, the third and fifth CO components in control mice are derived from cerebellar and thalamic structures, respectively. In contrast, the relationships among adjacent anatomical structures appear to break down in hMT1 mice producing components that are more difficult to interpret but suggestive of interactions among olivocerebellar and basal ganglia-cerebral cortical loops. For example, hMT1 GU component 2 includes loadings from the pontine nuclei (Pn), somatosensory and motor cortices, superior colliculus and substantia nigra

reticulata (SNR). Similarly, hMT1 GU component 3 includes sensory cortex (S2), thalamus (VM and VL), striatum (CPuRD) and IOM.

In total, scores for 20 components were calculated for each mouse using the loadings provided in Table 4. After Bonferroni correction for multiple comparisons, only Component 3 for GU in controls showed a significant difference between hMT1 and control mice (P = 0.0002). This component (Table 4) includes loadings from the IO (IOM and IOD), CHem, CVer and VL.

DISCUSSION

hMT1 mice do not exhibit overt manifestations of dystonia but do display abnormal behavioral phenotypes as well as neurochemical and electrophysiological abnormalities involving the basal ganglia (Sharma et al., 2005; Pisani et al., 2006; Balcioglu et al., 2007; Zhao et al., 2008; Sciamanna et al., 2009: Hewett et al. 2010). In this study, GU and CO activity served as approximate markers of acute and chronic metabolic activities in the brain, respectively. Our goal was to identify functional brain abnormalities in hMT1 transgenic mice, which may correlate with the already described behavioral, neurochemical and electrophysiological alterations identified in this DYT1 model. For comparisons with hMT1 mice, the control group included data from WT and hWT mice because hWT show negligible transgene expression (Zhao et al. 2008) and ROI GU and CO activity from hWT and WT were highly correlated. CO activity was significantly increased in the IOM and Purkinje cell layer of cerebellar cortex and decreased in caudal caudate-putamen, SNR, and MGP of hMT1 mice in comparison to the control group. Similarly, GU was significantly increased in IOM, IOD, and SNC, and decreased in MGP and LGP in hMT1 mice in comparison to the control group.

Not unexpectedly, the results of the two metabolic mapping methods employed herein did not generate identical results. Given that GU and CO activity measure distinct metabolic processes on different time scales, it is not surprising that these two methods generated both overlapping and unique results. Similar discrepancies between GU and CO metabolic patterns have also been reported in the mutant dystonic hamster (Nobrega et al., 1998; Richter et al., 1998). Moreover, functional neuroanatomical studies have shown that measures of GU and CO activity capture different aspects of network activity (Jacquin et al., 1993). Specifically, signals derived from CO histochemistry reflect oxidative energy metabolism of neural tissues, especially neurons and are concentrated at sites with greater mitochondrial density, whereas the signals derived from 2-DG autoradiography mainly reflect uptake of the tracer into astrocytes in synaptic regions with high Na+-K+-ATPase activity (Di Rocco et al., 1989; Wong-Riley, 1989; Gonzalez-Lima and Garrosa, 1991; Hevner et al., 1995; Magistretti and Pellerin, 1996; Tsacopoulos and Magistretti, 1996).

Overall, functional brain mapping in hMT1 mice demonstrated a shift of metabolic demand from the basal ganglia to the cerebellum (Fig. 4). In the basal ganglia, the decreased GU noted in the MGP and LGP might be due, in part, to decreased CO activity in CPu neurons, which send GABAergic projections to MGP, LGP and SNR. In MGP and SNR, CO was also reduced. These changes in CO activity in MGP and SNR mirror results in the dystonic hamster, in which significant decreases in CO activity were also found in the globus pallidus and substantia nigra reticulata (Nobrega et al., 1998). In agreement with these findings, independent studies in human subjects with generalized and focal dystonias have found significantly reduced mean GPi firing rates (Starr et al., 2005;Tang et al., 2007). Reduced GPi output to the thalamus might result in enhanced thalamocortical activation. In similar fashion, reduced SNR output might result in enhanced activity in the tectal and tegmental pathways, which receive inhibitory projections from SNR. Although likely associated, our

approach does not allow us to ascribe the hMT1 metabolic abnormalities in the basal ganglia to the increased nigrostriatal dopaminergic turnover described in hMT1 mice (Zhao et al., 2008).

Hypermetabolism in the cerebellar hemispheres has been reported in non-manifesting DYT1 carriers (Eidelberg, 1998; Trost et al., 2002; Carbon et al., 2004). Compatible with these results in humans, we identified hypermetabolism in the Purkinje cell layer (PCL), and, to a lesser degree, in the molecular layer of the cerebellum in hMT1 mice. In our model, increased GU and CO activity in the IO, which sends excitatory input to cerebellar Purkinje cells via the climbing fiber pathway, might alter the firing properties of Purkinje cells. In the dt rat, decreased complex spike firing rates are associated with rhythmic bursts of Purkinje cell simple spikes and a small increase in mean Purkinje cell firing rates (LeDoux and Lorden, 2002). In hMT1 mice, it is possible that increased activity of parallel fiber input to Purkinje cells activity outweighs the effects of increased climbing fiber activity. Alternatively, the olivocerebellar pathway in hMT1 mice could be defective at the post-synaptic level. Elevated Purkinje cell simple spike firing rates would be associated with enhanced metabolic activity at GABAergic synaptic terminals in the cerebellar nuclei; similar results have been identified in the dt rat (LeDoux, 2004). Although it is not possible to specifically attribute the previously reported gait abnormalities in hMT1 mice (Zhao et al., 2008) to dysfunction of either the basal ganglia or cerebellum, increased hind-base width is classically associated with dysfunction of the latter. Theoretically, this cerebellar abnormality could be either primary (Argyelan et al. 2009) or secondary to dysfunction of the basal ganglia (Zhao et al., 2008). In support of the latter possibility, functional imaging in DTY1 carriers suggests the possibility that a primary functional abnormality in the basal ganglia leads to compensatory maladaptive neural output from the cerebellum (Ghilardi et al., 2003; Carbon et al., 2008).

The IO may be a central node in communication between basal ganglia-thalamocortical and olivocerebellar circuits (Alexander and Crutcher, 1990; Marshall and Lang, 2004). The IO receives a wide variety of excitatory and GABAergic projections (Walberg, 1956, 1974; Berkley and Hand, 1978; Berkley and Worden, 1978; Saint-Cyr and Courville, 1981; Swenson and Castro, 1983). IO afferents arise from the spinal cord, medulla, pons, midbrain, cerebellar nuclei and cerebral cortex. Projections from the red nucleus, periaqueductal gray and other midbrain nuclei such as the interstitial nucleus of Cajal, nucleus of Bechterew and nucleus of Darkschewitsch enter the central tegmental tract, descend uncrossed, and terminate in the IO. Fibers, which ascend in the spinal cord, reach the IO either directly through the spino-olivary tract that courses through the anterior funiculus or indirectly via the dorsal column nuclei. Dysfunction of one or more of these afferents might induce hypermetabolism and altered neuronal activity in the IO. Alternatively, a defect intrinsic to the IO could be causally associated with the pathophysiology of DYT1 dystonia because climbing fiber dysfunction is critical to the dystonic movement disorders of the dt rat and rats treated with the neurotoxin 3-acetylpyridine (Sukin et al., 1987; LeDoux, 2004).

With a 2-DG autoradiography protocol similar to our own, striking increases in GU were detected in the cerebellar nuclei of the dt rat (Brown and Lorden, 1989). In the dt rat, correlations for GU in regions with known anatomical connections also suggested that basal ganglia efferents might be abnormal. The GU metabolism pattern identified in hMT1 transgenic mice show important qualitative similarities to patterns described in dt rats. However, the magnitude of the changes in hMT1 mice was small relative to alterations seen in the dt rat, possibly due to the fact that the latter model exhibits a profound generalized dystonia whereas the hMT1 mice do not display overt signs of dystonia. Unquestionably, the

cerebellum contributes to the dystonic movement disorder of the dt rat, which is eliminated by cerebellectomy (LeDoux et al., 1993; LeDoux et al., 1995).

Our correlation analysis supports the validity of our findings. In particular, the correlations that we obtained in control mice are similar to values previously reported in hamsters and rats (Brown and Lorden, 1989; Richter et al., 1998). A strong correlation between a specific nucleus and one of its synaptic targets, whether positive or negative, implies the presence of an important functional relationship (Wong-Riley, 1989; Wree, 1990). For specific examples, rats and hamsters show positive correlations between the cerebellar nuclei (medial and interpositus) and the red nucleus (Brown and Lorden, 1989). In addition, positive correlations between the striatum and LGP have been described in all three species of rodents (Brown and Lorden, 1989; Yamaguchi et al., 1992; Richter et al., 1998). These and several other correlations in control mice, including positive correlations of rostral caudate-putamen with MGP, positive correlations of rostral caudate-putamen with LGP, and negative correlations of the subthalamic nucleus with both MGP and LGP, were disrupted in hMT1 mice. Clearly, our data provides evidence that DYT1 dystonia is a network disorder with manifest metabolic aberrations in carriers of the DYT1 ΔGAG mutation.

Abbreviations

2-DG	2-deoxy-D-glucose
AInt	anterior interposed nucleus
CHem	cerebellar cortex hemisphere
CO	cytochrome oxidase
CPuC	caudate-putamen caudal
CPuRD	caudate-putamen rostral-dorsal
CPuRV	caudate-putamen rostral-ventral
CVer	cerebellar cortex vermis
hMT1	human mutant torsinA
hWT	human wild-type
IO	inferior olive
IOD	inferior olive dorsal accessory nucleus
IOM	inferior olive medial nucleus
Lat	lateral cerebellar nucleus
LGP	lateral globus pallidus
Med	medial cerebellar nucleus
MGP	medial globus pallidus
O.D.	optical density
PB	phosphate buffer
PET	positron emission tomography
RMC	red nucleus magnocellular
ROI	region of interest
SNC	substantia nigra compacta

STh	subthalamic nucleus
VL	ventrolateral thalamic nucleus
VM	ventromedial thalamic nucleus
WT	wild-type

Acknowledgments

This work was supported by the Dystonia Medical Research Foundation and the National Institute of Neurological Diseases and Stroke (R01NS048458, R03NS050185, R01NS069936).

REFERENCES

Alexander GE, Crutcher MD. Functional architecture of basal ganglia circuits: neural substrates of parallel processing. Trends Neurosci. 1990; 13:266–271. [PubMed: 1695401]

Argyelan M, Carbon M, Niethammer M, Ulug AM, Voss HU, Bressman SB, Dhawan V, Eidelberg D. Cerebellothalamocortical connectivity regulates penetrance in dystonia. J Neurosci. 2009; 29:9740–9747. [PubMed: 19657027]

Asanuma K, Ma Y, Okulski J, Dhawan V, Chaly T, Carbon M, Bressman SB, Eidelberg D. Decreased striatal D2 receptor binding in non-manifesting carriers of the DYT1 dystonia mutation. Neurology. 2005; 64:347–349. [PubMed: 15668438]

Augood SJ, Hollingsworth Z, Albers DS, Yang L, Leung JC, Muller B, Klein C, Breakefield XO, Standaert DG. Dopamine transmission in DYT1 dystonia: a biochemical and autoradiographical study. Neurology. 2002; 59:445–448. [PubMed: 12177384]

Balcioglu A, Kim MO, Sharma N, Cha JH, Breakefield XO, Standaert DG. Dopamine release is impaired in a mouse model of DYT1 dystonia. J Neurochem. 2007; 102:783–788. [PubMed: 17550429]

Berkley KJ, Hand PJ. Projections to the inferior olive of the cat. II. Comparisons of input from the gracile, cuneate and the spinal trigeminal nuclei. J Comp Neurol. 1978; 180:253–264. [PubMed: 659661]

Berkley KJ, Worden IG. Projections to the inferior olive of the cat. I. Comparisons of input from the dorsal column nuclei, the lateral cervical nucleus, the spino-olivary pathways, the cerebral cortex and the cerebellum. J Comp Neurol. 1978; 180:237–251. [PubMed: 659660]

Bressman SB, de Leon D, Raymond D, Ozelius LJ, Breakefield XO, Nygaard TG, Almasy L, Risch NJ, Kramer PL. Clinical-genetic spectrum of primary dystonia. Adv Neurol. 1998; 78:79–91. [PubMed: 9750905]

Bressman SB, Sabatti C, Raymond D, de Leon D, Klein C, Kramer PL, Brin MF, Fahn S, Breakefield X, Ozelius LJ, Risch NJ. The DYT1 phenotype and guidelines for diagnostic testing. Neurology. 2000; 54:1746–1752. [PubMed: 10802779]

Brown LL, Lorden JF. Regional cerebral glucose utilization reveals widespread abnormalities in the motor system of the rat mutant dystonic. J Neurosci. 1989; 9:4033–4041. [PubMed: 2585066]

Carbon M, Su S, Dhawan V, Raymond D, Bressman S, Eidelberg D. Regional metabolism in primary torsion dystonia: effects of penetrance and genotype. Neurology. 2004; 62:1384–1390. [PubMed: 15111678]

Carbon M, Ghilardi MF, Argyelan M, Dhawan V, Bressman SB, Eidelberg D. Increased cerebellar activation during sequence learning in DYT1 carriers: an equiperformance study. Brain. 2008; 131:146–154. [PubMed: 17947338]

Di Rocco RJ, Kageyama GH, Wong-Riley MT. The relationship between CNS metabolism and cytoarchitecture: a review of 14C-deoxyglucose studies with correlation to cytochrome oxidase histochemistry. Comput Med Imaging Graph. 1989; 13:81–92. [PubMed: 2538221]

Duncan GE, Stumpf WE. Brain activity patterns: assessment by high resolution autoradiographic imaging of radiolabeled 2-deoxyglucose and glucose uptake. Prog Neurobiol. 1991; 37:365–382. [PubMed: 1758965]

Eidelberg D. Abnormal brain networks in DYT1 dystonia. Adv Neurol. 1998; 78:127–133. [PubMed: 9750910]

Fahn S. Concept and classification of dystonia. Adv Neurol. 1988; 50:1–8. [PubMed: 3041755]

Franklin, K.; Paxinos, G. The mouse brain atlas in stereotaxic coordinates. San Diego: Academic Press; 1997.

Ghilardi MF, Carbon M, Silvestri G, Dhawan V, Tagliati M, Bressman S, Ghez C, Eidelberg D. Impaired sequence learning in carriers of the DYT1 dystonia mutation. Ann Neurol. 2003; 54:102–109. [PubMed: 12838525]

Gonzalez-Lima F, Garrosa M. Quantitative histochemistry of cytochrome oxidase in rat brain. Neurosci Lett. 1991; 123:251–253. [PubMed: 1709270]

Gonzalez-Lima F, Jones D. Quantitative mapping of cytochrome oxidase activity in the central auditory system of the gerbil: a study with calibrated activity standards and metal-intensified histochemistry. Brain Res. 1994; 660:34–49. [PubMed: 7828000]

Hess HH, Pope A. Ultramicrospectrophotometric determination of cytochrome oxidase for quantitative histochemistry. J Biol Chem. 1953; 204:295–306. [PubMed: 13084602]

Hevner RF, Liu S, Wong-Riley MT. A metabolic map of cytochrome oxidase in the rat brain: histochemical, densitometric and biochemical studies. Neuroscience. 1995; 65:313–342. [PubMed: 7777153]

Hewett J, Johanson P, Sharma N, Standaert D, Balcioglu A. Function of dopamine transporter is compromised in DYT1 transgenic animal model in vivo. J Neurochem. 2010; 113:228–235. [PubMed: 20132487]

Jacquin MF, McCasland JS, Henderson TA, Rhoades RW, Woolsey TA. 2-DG uptake patterns related to single vibrissae during exploratory behaviors in the hamster trigeminal system. J Comp Neurol. 1993; 332:38–58. [PubMed: 8390494]

Kimura H, McGeer EG, McGeer PL. Metabolic alterations in an animal model of Huntington's disease using the 14C-deoxyglucose method. J Neural Transm. 1980 Suppl:103–109.

LeDoux, MS. Animal Models of Movement Disorders. Amsterdam, Netherlands: Elsevier; 2004.

LeDoux MS, Lorden JF. Abnormal spontaneous and harmaline-stimulated Purkinje cell activity in the awake genetically dystonic rat. Exp Brain Res. 2002; 145:457–467. [PubMed: 12172657]

LeDoux MS, Lorden JF, Ervin JM. Cerebellectomy eliminates the motor syndrome of the genetically dystonic rat. Exp Neurol. 1993; 120:302–310. [PubMed: 8491286]

LeDoux MS, Lorden JF, Meinzen-Derr J. Selective elimination of cerebellar output in the genetically dystonic rat. Brain Res. 1995; 697:91–103. [PubMed: 8593599]

Magistretti PJ, Pellerin L. Cellular bases of brain energy metabolism and their relevance to functional brain imaging: evidence for a prominent role of astrocytes. Cereb Cortex. 1996; 6:50–61. [PubMed: 8670638]

Marshall SP, Lang EJ. Inferior olive oscillations gate transmission of motor cortical activity to the cerebellum. J Neurosci. 2004; 24:11356–11367. [PubMed: 15601942]

McCasland, JS.; Graczyk, GM. Curr Protoc Neurosci. New York: John Wiley & Sons, Inc.; 2001. Metabolic mapping.

McCasland JS, Woolsey TA. New high-resolution 2-deoxyglucose method featuring double labeling and automated data collection. J Comp Neurol. 1988; 278:543–554. [PubMed: 3068265]

Mitchell IJ, Boyce S, Sambrook MA, Crossman AR. A 2-deoxyglucose study of the effects of dopamine agonists on the parkinsonian primate brain. Implications for the neural mechanisms that mediate dopamine agonist-induced dyskinesia. Brain. 1992; 115(Pt 3):809–824. [PubMed: 1628204]

Nobrega JN, Richter A, Jiwa D, Raymond R, Loscher W. Regional alterations in neuronal activity in dystonic hamster brain determined by quantitative cytochrome oxidase histochemistry. Neuroscience. 1998; 83:1215–1223. [PubMed: 9502259]

Ozelius LJ, Hewett JW, Page CE, Bressman SB, Kramer PL, Shalish C, de Leon D, Brin MF, Raymond D, Corey DP, Fahn S, Risch NJ, Buckler AJ, Gusella JF, Breakefield XO. The early-onset torsion dystonia gene (DYT1) encodes an ATP-binding protein. Nat Genet. 1997; 17:40–48. [PubMed: 9288096]

Pisani A, Martella G, Tscherter A, Bonsi P, Sharma N, Bernardi G, Standaert DG. Altered responses to dopaminergic D2 receptor activation and N-type calcium currents in striatal cholinergic interneurons in a mouse model of DYT1 dystonia. Neurobiol Dis. 2006; 24:318–325. [PubMed: 16934985]

Redies C, Gjedde A. Double-label and conventional deoxyglucose methods: a practical guide for the user. Cerebrovasc Brain Metab Rev. 1989; 1:319–367. [PubMed: 2701657]

Richter A, Brotchie JM, Crossman AR, Loscher W. [3H]-2-deoxyglucose uptake study in mutant dystonic hamsters: abnormalities in discrete brain regions of the motor system. Mov Disord. 1998; 13:718–725. [PubMed: 9686781]

Saint-Cyr JA, Courville J. Sources of descending afferents to the inferior olive from the upper brain stem in the cat as revealed by the retrograde transport of horseradish peroxidase. J Comp Neurol. 1981; 198:567–581. [PubMed: 7251931]

Sciamanna G, Bonsi P, Tassone A, Cuomo D, Tscherter A, Viscomi MT, Martella G, Sharma N, Bernardi G, Standaert DG, Pisani A. Impaired striatal D2 receptor function leads to enhanced GABA transmission in a mouse model of DYT1 dystonia. Neurobiol Dis. 2009; 34:133–145. [PubMed: 19187797]

Sharma N, Baxter MG, Petravicz J, Bragg DC, Schienda A, Standaert DG, Breakefield XO. Impaired motor learning in mice expressing torsinA with the DYT1 dystonia mutation. J Neurosci. 2005; 25:5351–5355. [PubMed: 15930383]

Silverman MS, Tootell RB. Modified technique for cytochrome oxidase histochemistry: increased staining intensity and compatibility with 2-deoxyglucose autoradiography. J Neurosci Methods. 1987; 19:1–10. [PubMed: 2434810]

Starr PA, Rau GM, Davis V, Marks WJ Jr, Ostrem JL, Simmons D, Lindsey N, Turner RS. Spontaneous pallidal neuronal activity in human dystonia: comparison with Parkinson's disease and normal macaque. J Neurophysiol. 2005; 93:3165–3176. [PubMed: 15703229]

Sukin D, Skedros DG, Beales M, Stratton SE, Lorden JF, Oltmans GA. Temporal sequence of motor disturbances and increased cerebellar glutamic acid decarboxylase activity following 3-acetylpyridine lesions in adult rats. Brain Res. 1987; 426:82–92. [PubMed: 3690321]

Swenson RS, Castro AJ. The afferent connections of the inferior olivary complex in rats: a study using the retrograde transport of horseradish peroxidase. Am J Anat. 1983; 166:329–341. [PubMed: 6846209]

Tang JK, Moro E, Mahant N, Hutchison WD, Lang AE, Lozano AM, Dostrovsky JO. Neuronal firing rates and patterns in the globus pallidus internus of patients with cervical dystonia differ from those with Parkinson's disease. J Neurophysiol. 2007; 98:720–729. [PubMed: 17537900]

Trost M, Carbon M, Edwards C, Ma Y, Raymond D, Mentis MJ, Moeller JR, Bressman SB, Eidelberg D. Primary dystonia: is abnormal functional brain architecture linked to genotype? Ann Neurol. 2002; 52:853–856. [PubMed: 12447944]

Tsacopoulos M, Magistretti PJ. Metabolic coupling between glia and neurons. J Neurosci. 1996; 16:877–885. [PubMed: 8558256]

Vila M, Levy R, Herrero MT, Faucheux B, Obeso JA, Agid Y, Hirsch EC. Metabolic activity of the basal ganglia in parkinsonian syndromes in human and non-human primates: a cytochrome oxidase histochemistry study. Neuroscience. 1996; 71:903–912. [PubMed: 8684621]

Walberg F. Descending connections to the inferior olive; an experimental study in the cat. J Comp Neurol. 1956; 104:77–173. [PubMed: 13306830]

Walberg F. Descending connections from the mesencephalon to the inferior olive: an experimental study in the cat. Exp Brain Res. 1974; 20:145–156. [PubMed: 4134870]

Wong-Riley MT. Cytochrome oxidase: an endogenous metabolic marker for neuronal activity. Trends Neurosci. 1989; 12:94–101. [PubMed: 2469224]

Wree A. Principles of the 2-deoxyglucose method for the determination of the local cerebral glucose utilization. Eur J Morphol. 1990; 28:132–138. [PubMed: 2245129]

Wree A, Schleicher A. The determination of the local cerebral glucose utilization with the 2-deoxyglucose method. Histochemistry. 1988; 90:109–121. [PubMed: 3068213]

Xiao J, Bastian RW, Perlmutter JS, Racette BA, Tabbal SD, Karimi M, Paniello RC, Blitzer A, Batish SD, Wszolek ZK, Uitti RJ, Hedera P, Simon DK, Tarsy D, Truong DD, Frei KP, Pfeiffer RF,

Gong S, Zhao Y, LeDoux MS. High-throughput mutational analysis of TOR1A in primary dystonia. BMC Med Genet. 2009; 10:24. [PubMed: 19284587]

Yamaguchi T, Kato M, Fukui M, Akazawa K. Rolling mouse Nagoya as a mutant animal model of basal ganglia dysfunction: determination of absolute rates of local cerebral glucose utilization. Brain Res. 1992; 598:38–44. [PubMed: 1486501]

Zhao Y, Decuypere M, Ledoux MS. Abnormal motor function and dopamine neurotransmission in DYT1 DeltaGAG transgenic mice. Exp Neurol. 2008; 210:719–730. [PubMed: 18299128]

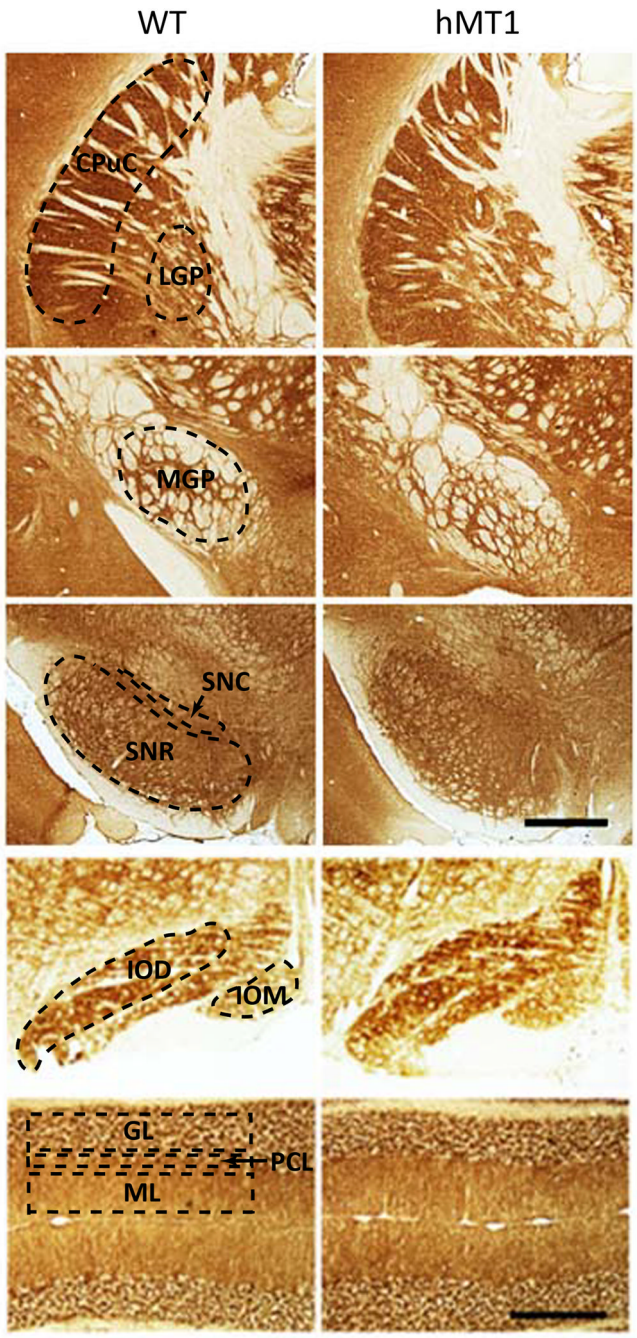

Fig. 1.

CO histochemical labeling of CPu, MGP, SNR, IO and cerebellar cortex (CB) in hMT1 mice and WT littermates. Selected ROIs (CPuC, LGP, MGP, SNC, SNR, IOD, IOM, ML, PCL, and GL) are demarcated with hashed lines. Scale bars, 100 μm.

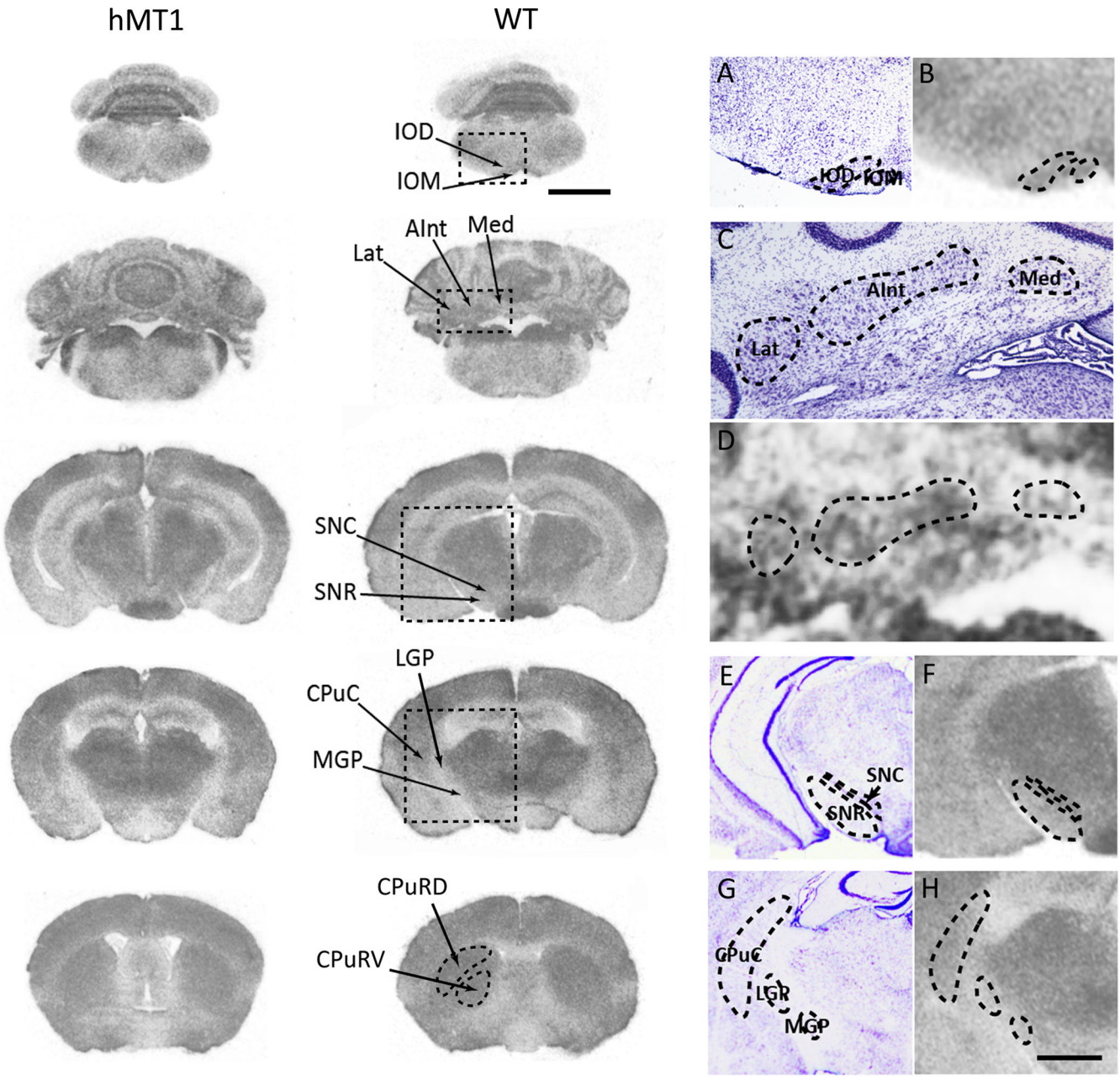

Fig. 2.

Representative GU autoradiographic images for hMT1 and WT mice. ROIs (IOD, IOM, Lat, AInt, Med, SNC, SNR, CpuC, LGP, MGP, CPu) are pointed out with arrows (scale bar, 2 mm). Selected ROIs are demarcated with hashed lines in magnified images and contiguous cresyl violet-stained sections (scale bars: 300 μm for A and B; 500 μm for C and D; and 1 mm for E, F, G, and H).

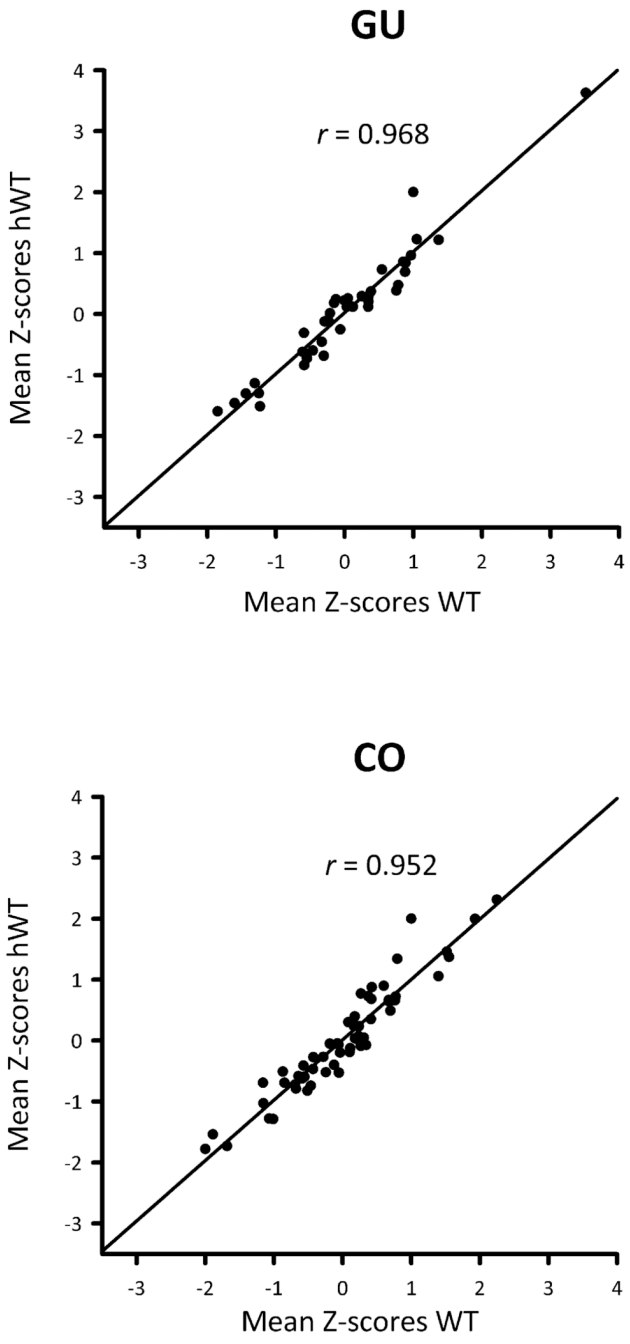

Fig. 3.
GU and CO Z-score scatter plots for WT and hWT mice.

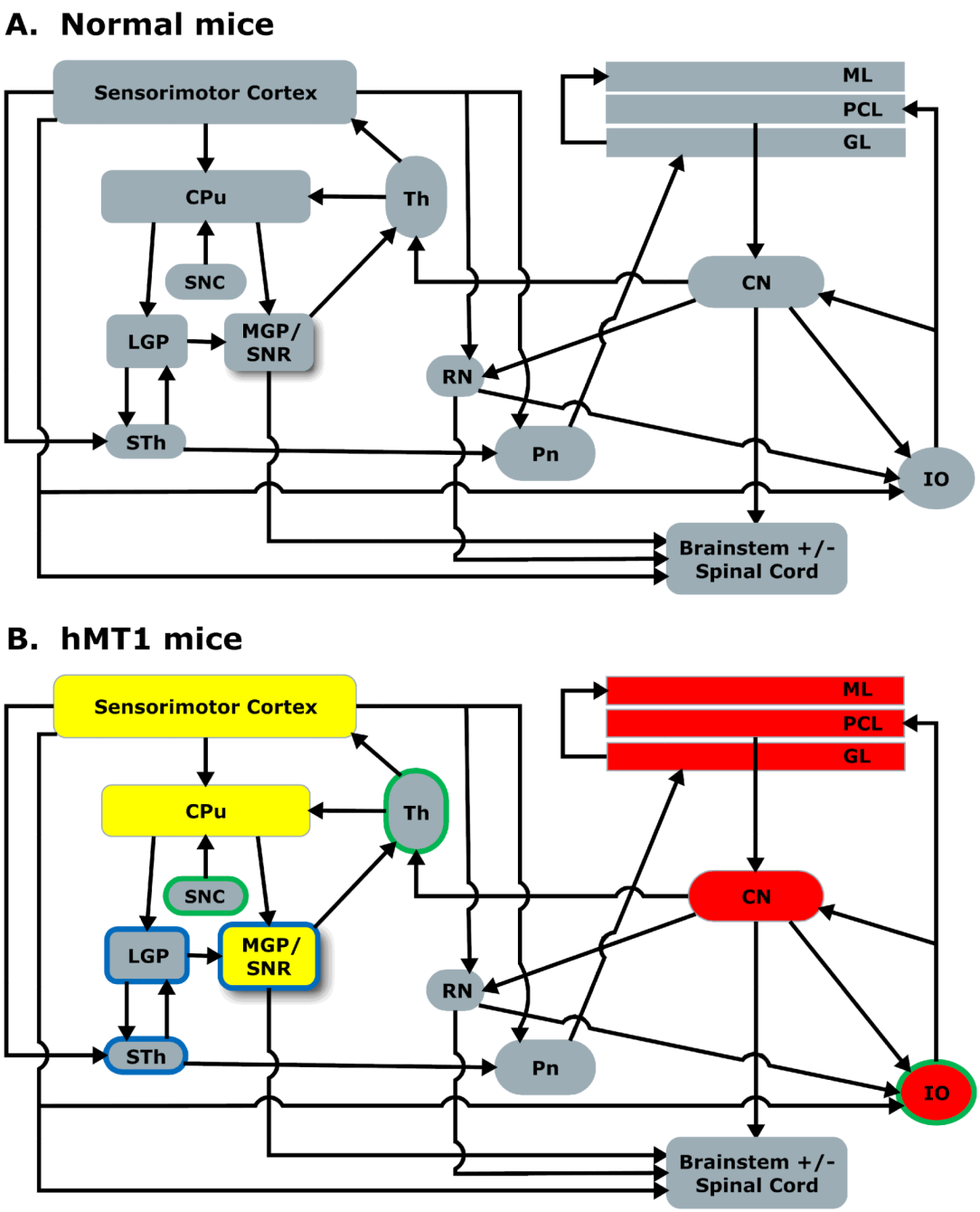

Fig. 4.

A. Sensorimotor network model in normal mice. B. Sensorimotor network model in hMT1 mice based on GU and CO activity. Red and yellow fills denote increased and decreased CO activity, respectively. Green and blue borders denote increased and decreased GU respectively. To facilitate overall understanding of the experimental findings, select anatomical structures (e.g., sensorimotor cortex, cerebellar nuclei [CN], thalamus [Th] and red nucleus [RN]) are represented in place of their multiple formative ROIs, and the effects of genotype (hMT1) with $P < 0.05$ are included in Fig. 4B. CN, cerebellar nuclei; Th, thalamus; RN, red nucleus. Other abbreviations are defined in the text and tables.

Table 1

GU in hMT1 mice

	*P** (Z-score)	GU (nCi/g)		Z-score	
		control	hMT1	control	hMT1
MGP (medial globus pallidus)	0.0009	164.84 ± 11.91	154.64 ± 12.09	−1.54 ± 0.06	−1.89 ± 0.06
IOM (inferior olive, medial nucleus)	0.0017	225.91 ± 13.23	269.48 ± 18.13	−0.61 ± 0.07	−0.23 ± 0.07
IOD (inferior olive, dorsal accessory nucleus)	0.0049	183 ± 13.41	220.78 ± 14.27	−1.27 ± 0.08	−0.93 ± 0.07
SNC (substantia nigra compacta)	0.0064	235.33 ± 14.85	271.21 ± 16.43	−0.47 ± 0.08	−0.21 ± 0.04
LGP (lateral globus pallidus)	0.0098	184.25 ± 11.95	182.5 ± 14.19	−1.24 ± 0.06	−1.49 ± 0.07
VM (ventromedial thalamic nucleus)	0.0211	282.09 ± 16.73	321.88 ± 18	0.25 ± 0.06	0.55 ± 0.1
IPC (interpeduncular nucleus, caudal subnucleus)	0.0263	305.68 ± 20.73	305.04 ± 20.69	0.6 ± 0.11	0.28 ± 0.07
STh (subthalamic nucleus)	0.0447	284.99 ± 16.96	295.72 ± 19.07	0.29 ± 0.05	0.14 ± 0.05
Lat (lateral cerebellar nucleus)	0.0678	286.87 ± 16.52	320.02 ± 20.51	0.32 ± 0.08	0.49 ± 0.04
RMC (red nucleus magnocellular)	0.0966	283.83 ± 16.57	294.31 ± 21.4	0.27 ± 0.03	0.11 ± 0.08
CHem (cerebellar cortex, hemisphere)	0.1001	224.74 ± 13.66	251.99 ± 16.94	−0.62 ± 0.04	−0.49 ± 0.06
CVer (cerebellar cortex, vermis)	0.1107	240.14 ± 12.99	270.75 ± 17.24	−0.39 ± 0.06	−0.21 ± 0.08
SO (supraoptic nucleus)	0.1705	350.22 ± 17.8	346.05 ± 18.6	1.3 ± 0.13	0.91 ± 0.24
S2 (secondary somatosensory cortex)	0.1816	269.37 ± 15.03	281.07 ± 16.75	0.07 ± 0.07	−0.06 ± 0.05
Med (medial cerebellar nucleus)	0.1858	273.69 ± 15.92	303.08 ± 19.09	0.12 ± 0.09	0.25 ± 0.03
Cg (cingulum)	0.2216	271.43 ± 15.95	279.64 ± 21.04	0.09 ± 0.11	−0.1 ± 0.11
VL (ventrolateral thalamic nucleus)	0.2325	256.73 ± 15.8	286.89 ± 17.51	−0.14 ± 0.08	0.06 ± 0.14
SC (superior colliculus)	0.2957	226.78 ± 17.49	232.41 ± 17.57	−0.62 ± 0.12	−0.77 ± 0.07
PAG (periaqueductal gray)	0.2965	150.44 ± 10.3	157.52 ± 13.81	−1.74 ± 0.08	−1.85 ± 0.06
AInt (anterior interpositus nucleus)	0.3024	290.78 ± 16.6	320.08 ± 22.12	0.38 ± 0.07	0.48 ± 0.06
M1 (primary motor cortex)	0.3591	254.09 ± 14.81	277.18 ± 17.29	−0.18 ± 0.06	−0.11 ± 0.05
DLG (dorsal lateral geniculate nucleus)	0.3612	308.64 ± 18.71	320.94 ± 17.74	0.65 ± 0.09	0.52 ± 0.1
Pn (pontine nuclei)	0.4041	178.05 ± 15.44	200.94 ± 18.82	−1.35 ± 0.09	−1.23 ± 0.1
IC (inferior colliculus)	0.4431	500.71 ± 24.13	546.82 ± 41.84	3.56 ± 0.1	3.71 ± 0.15
SNR (substantia nigra reticulata)	0.4765	176.44 ± 15.04	183.86 ± 16.81	−1.38 ± 0.09	−1.47 ± 0.09
PnO (pontine reticular nucleus oral)	0.5250	220.91 ± 17.16	243.15 ± 16.44	−0.69 ± 0.07	−0.62 ± 0.09
M2 (secondary motor cortex)	0.5264	283.14 ± 15.73	300.19 ± 20.64	0.27 ± 0.09	0.2 ± 0.06

	*P** (Z-score)	GU (nCi/g)		Z-score	
		control	hMT1	control	hMT1
S1BF (somatosensory 1, barrel field)	0.5652	320.91 ± 16.57	338.78 ± 19.07	0.86 ± 0.08	0.78 ± 0.09
LC (locus coeruleus)	0.6665	230.53 ± 14.07	256.78 ± 21.73	−0.52 ± 0.1	−0.44 ± 0.17
CPuRV (caudate-putamen, rostral-ventral)	0.6760	258.39 ± 16.79	271.97 ± 15.75	−0.12 ± 0.1	−0.18 ± 0.1
VP (ventral pallidum)	0.7482	318.19 ± 17.07	337.13 ± 17.19	0.8 ± 0.08	0.77 ± 0.08
MVe (medial vestibular nucleus)	0.7626	323.03 ± 18.28	349.86 ± 24.12	0.87 ± 0.08	0.92 ± 0.14
RMg (raphe magnus nucleus)	0.7691	235.12 ± 16.58	250.19 ± 17.96	−0.47 ± 0.12	−0.52 ± 0.13
CPuC (caudate-putamen, caudal)	0.7997	251.74 ± 14.78	271.14 ± 14.94	−0.22 ± 0.08	−0.19 ± 0.08
DC (dorsal cochlear nucleus)	0.8153	306.96 ± 16.08	325.65 ± 24.74	0.62 ± 0.11	0.57 ± 0.21
VA (ventral anterior thalamic nucleus)	0.9403	339.91 ± 19.22	362.17 ± 17.83	1.13 ± 0.08	1.14 ± 0.16
S1HL (somatosensory 1, hindlimb region)	0.9541	264.41 ± 14.87	285.63 ± 22.4	−0.01 ± 0.09	−0.02 ± 0.09
LVe (lateral vestibular nucleus)	0.9581	330.62 ± 19.6	351.85 ± 20.72	0.97 ± 0.07	0.96 ± 0.08
CPuRD (caudate-putamen, rostral-dorsal)	0.9745	274.32 ± 14.68	294.23 ± 17.14	0.14 ± 0.09	0.13 ± 0.04
S1FL (somatosensory 1, forelimb region)	0.9952	267.1 ± 14.73	287.52 ± 18.82	0.03 ± 0.09	0.03 ± 0.07

*data was derived from 8 hMT1, 6 hWT and 8 WT mice.

Table 2

CO activity in hMT1 mice

	P (Z-score)	CO activity (μmol/min/g)		Z-score	
		Control	hMT1	Control	hMT1
CPuC (caudate-putamen, caudal)	0.0008	41.43 ± 1.92	39.98 ± 2.64	1.49 ± 0.09	0.94 ± 0.1
SNR (substantia nigra reticulata)	0.0025	24.61 ± 1.69	25.86 ± 2.06	−0.61 ± 0.05	−0.84 ± 0.04
IOM (inferior olive, medial nucleus)	0.0059	20.15 ± 2.54	28.85 ± 2.17	−1.14 ± 0.18	−0.44 ± 0.15
PCL (Purkinje cell layer, cerebellum)	0.0074	35.53 ± 2.16	44.04 ± 2.94	0.75 ± 0.11	1.47 ± 0.2
MGP (medial globus pallidus)	0.0097	15.83 ± 1.07	16.09 ± 1.34	−1.71 ± 0.09	−2.06 ± 0.08
GL (granule cell layer, cerebellum)	0.0102	27.26 ± 1.78	33.32 ± 2.49	−0.27 ± 0.09	0.12 ± 0.11
S1HL (somatosensory 1, hindlimb region)	0.0107	35.19 ± 1.96	34.57 ± 2.57	0.68 ± 0.08	0.27 ± 0.12
VLG (ventrolateral geniculate nucleus)	0.0134	28.7 ± 2.16	28.43 ± 2.12	−0.11 ± 0.07	−0.49 ± 0.11
ML (molecular layer, cerebellum)	0.0165	31.17 ± 2.08	38.71 ± 2.67	0.2 ± 0.09	0.79 ± 0.19
S1FL (somatosensory 1, forelimb region)	0.0244	34.94 ± 1.81	34.67 ± 2.54	0.67 ± 0.07	0.29 ± 0.13
IOD (inferior olive, dorsal accessory nucleus)	0.0307	19.77 ± 1.74	27.49 ± 2.16	−1.17 ± 0.11	−0.59 ± 0.21
Lat (lateral cerebellar nucleus)	0.0340	35.38 ± 2.96	43.32 ± 3.69	0.74 ± 0.19	1.32 ± 0.18
Po (posterior thalamic nuclear group)	0.0619	31.92 ± 2.08	32.45 ± 3.1	0.28 ± 0.09	−0.04 ± 0.13
CPuRV (caudate-putamen, rostral-ventral)	0.0786	41.33 ± 1.94	40.97 ± 2.95	1.47 ± 0.15	1.06 ± 0.16
AInt (anterior interposed nucleus)	0.0791	33.51 ± 2.7	40.4 ± 3.86	0.5 ± 0.17	0.94 ± 0.16
Rt (reticular thalamic nucleus)	0.0804	25.61 ± 1.64	26.05 ± 2.35	−0.49 ± 0.08	−0.83 ± 0.16
CPuRD (caudate-putamen, rostral-dorsal)	0.0885	31.48 ± 1.59	31.85 ± 2.42	0.24 ± 0.14	−0.08 ± 0.11
Med (medial cerebellar nucleus)	0.0929	21.67 ± 2.07	27.99 ± 2.8	−0.94 ± 0.12	−0.61 ± 0.14
DC (dorsal cochlear nucleus)	0.1554	26.33 ± 3.05	34.94 ± 4.26	−0.35 ± 0.24	0.26 ± 0.33
LGP (lateral globus pallidus)	0.1556	23.86 ± 1.42	25.14 ± 2.09	−0.71 ± 0.09	−0.93 ± 0.12
BLA (basolateral amygdaloid nucleus, anterior)	0.1609	33.93 ± 1.83	34.67 ± 3.08	0.54 ± 0.11	0.27 ± 0.15
Cg (cingulum)	0.1950	33.9 ± 2.05	34.32 ± 2.64	0.54 ± 0.13	0.26 ± 0.17
S1BF (somatosensory 1, barrel field)	0.2624	33.93 ± 1.82	36.64 ± 3.02	0.66 ± 0.11	0.51 ± 0.06
CA3poly (polymorphic layer of CA3)	0.2739	29.13 ± 1.93	30.79 ± 3.05	−0.07 ± 0.09	−0.23 ± 0.11
IPC (interpeduncular nucleus,caudal subnucleus)	0.2914	28.46 ± 2.33	34.19 ± 2.62	−0.06 ± 0.17	0.23 ± 0.2
VP (ventral pallidum)	0.3551	34.64 ± 1.98	38.59 ± 3.19	0.64 ± 0.08	0.75 ± 0.09
M2 (secondary motor cortex)	0.3690	31.66 ± 1.61	32.39 ± 2.4	0.38 ± 0.12	0.18 ± 0.17

	P (Z-score)	CO activity (μmol/min/g)		Z-score	
		Control	hMT1	Control	hMT1
SNC (substantia nigra compacta)	0.3727	25 ± 1.96	26.9 ± 2.25	−0.57 ± 0.08	−0.69 ± 0.11
LVe (lateral vestibular nucleus)	0.4091	20.38 ± 2.33	25.22 ± 2.2	−1.09 ± 0.14	−0.92 ± 0.14
M1 (primary motor cortex)	0.4282	34.13 ± 1.64	35.08 ± 2.86	0.71 ± 0.14	0.51 ± 0.19
Pn (pontine nuclei)	0.4504	15.33 ± 2.06	16.81 ± 1.98	−1.74 ± 0.12	−1.94 ± 0.23
S2 (secondary somatosensory cortex)	0.4983	30.23 ± 1.65	33.04 ± 2.63	0.19 ± 0.13	0.07 ± 0.13
VL (ventrolateral thalamic nucleus)	0.5029	24.91 ± 1.95	27.68 ± 2.45	−0.59 ± 0.1	−0.48 ± 0.11
SO (supraoptic nucleus)	0.5648	28.71 ± 1.99	30.66 ± 2.86	−0.12 ± 0.11	−0.23 ± 0.15
SR (stratum radiatum, CA1)	0.5687	26.15 ± 1.95	28.01 ± 2.61	−0.45 ± 0.12	−0.56 ± 0.15
LSO (lateral superior olive)	0.5688	30.4 ± 2.66	35.61 ± 3.47	0.19 ± 0.2	0.39 ± 0.28
VM (ventromedial thalamic nucleus)	0.6376	26.65 ± 2.11	28.01 ± 2.34	−0.37 ± 0.09	−0.42 ± 0.04
CIC (central nucleus, inferior colliculus)	0.6513	39.22 ± 2.93	43.94 ± 4.21	1.24 ± 0.24	1.4 ± 0.26
H (hilus dentate gyrus)	0.6877	23.76 ± 1.77	26.18 ± 2.83	−0.73 ± 0.1	−0.8 ± 0.14
PAG (periaqueductal gray)	0.6918	24.6 ± 1.93	27.39 ± 2.29	−0.6 ± 0.08	−0.65 ± 0.08
PnO (pontine reticular nucleus oral)	0.6939	23.93 ± 2.01	27.42 ± 2.17	−0.7 ± 0.08	−0.65 ± 0.1
MG (medial geniculate nucleus)	0.7019	30.79 ± 2.1	33.44 ± 2.72	0.16 ± 0.12	0.1 ± 0.1
MVe (medial vestibular nucleus)	0.7160	23.84 ± 3.29	26.68 ± 4.56	−0.66 ± 0.25	−0.82 ± 0.34
InG (intermediate gray, superior colliculus)	0.7260	30.84 ± 2.2	33.11 ± 3.04	0.15 ± 0.1	0.07 ± 0.18
LD (laterodorsal thalamic nucleus)	0.7709	29.4 ± 2.45	31.91 ± 2.75	−0.03 ± 0.1	−0.08 ± 0.13
STh (subthalamic nucleus)	0.7822	45.46 ± 2.83	48.49 ± 3.17	1.96 ± 0.11	2.02 ± 0.16
oDG (outer blade, dentate gyrus)	0.7907	27.46 ± 2.26	30.07 ± 2.47	−0.25 ± 0.12	−0.29 ± 0.09
RMC (red nucleus magnocellular)	0.8004	37.59 ± 1.91	41.37 ± 2.91	1.05 ± 0.19	1.15 ± 0.33
RMg (raphe magnus)	0.8558	14.08 ± 1.24	17.13 ± 1.98	−1.9 ± 0.1	−1.93 ± 0.12
DLG (dorsal lateral geniculate nucleus)	0.8705	30.58 ± 2.21	33.17 ± 2.62	0.11 ± 0.08	0.09 ± 0.11
VA (ventral anterior thalamic nucleus)	0.8779	30.58 ± 2.37	32.15 ± 2.51	0.1 ± 0.1	0.12 ± 0.06
SLM (stratum lacunosum-moleculare CA1)	0.8799	47.88 ± 2.72	50.19 ± 3.61	2.28 ± 0.15	2.25 ± 0.15
APTD (anterior pretectal nucleus, dorsal part)	0.9056	29.76 ± 2.19	32.6 ± 2.84	0 ± 0.08	0.02 ± 0.14
LC (locus coeruleus)	0.9447	23.39 ± 2.14	26.58 ± 2.59	−0.77 ± 0.11	−0.76 ± 0.13
iDG (inner blade, dentate gyrus)	0.9558	34.61 ± 2.36	37.44 ± 3.33	0.6 ± 0.14	0.61 ± 0.13
SuG (superficial gray, superior colliculus)	0.9956	27.45 ± 2.02	30.31 ± 3.11	−0.28 ± 0.13	−0.28 ± 0.2

*data was derived from 9 hMT1, 8 hWT and 9 WT mice.

Table 3

Metabolic correlations between neuroanatomically-connected nuclei in hMT1 mice

	Cytochrome Oxidase Activity				Glucose Utilization			
	Control		hMT1		Control		hMT1	
ROIs	r*	*P*	r*	*P*	r*	*P*	r*	*P*
AInt/RMC	0.54	0.0274	−0.01	0.9820	0.16	0.5821	0.52	0.1903
Lat/RMC	0.34	0.1873	0.06	0.8723	0.12	0.6831	0.22	0.6054
AInt/VL	−0.31	0.2257	−0.50	0.3104	−0.62	0.0189	−0.56	0.1479
Lat/VL	−0.24	0.3437	−0.31	0.5444	0.79	0.0008	−0.41	0.3178
Lat/VM	−0.25	0.3328	−0.001	0.9978	0.49	0.0758	−0.43	0.2825
IOM/Med	0.33	0.1914	−0.13	0.7313	0.21	0.4787	0.11	0.7953
IOD/AInt	0.15	0.5607	−0.11	0.7735	0.23	0.4317	0.27	0.5186
IOM/CVer	-	-	-	-	0.03	0.2935	−0.14	0.7397
CVer/Med	-	-	-	-	0.24	0.4129	0.57	0.1383
CHem/Lat	-	-	-	-	0.27	0.3552	0.25	0.5560
MGP/VA	−0.05	0.8377	−0.16	0.7690	−0.16	0.5797	0.27	0.5139
SNR/VA	−0.08	0.7634	0.44	0.3870	−0.14	0.6257	−0.43	0.2928
LGP/MGP	0.75	0.0005	0.61	0.0792	0.42	0.1395	0.38	0.3472
LGP/SNR	0.35	0.1675	0.19	0.6169	−0.46	0.0981	−0.42	0.3028
STh/MGP	−0.46	0.0606	0.39	0.2932	0.09	0.7662	0.43	0.2850
STh/SNR	−0.07	0.7969	−0.12	0.7637	−0.16	0.5849	−0.27	0.5146
STh/LGP	−0.39	0.1225	0.61	0.0834	0.02	0.9467	−0.17	0.6796
CPuRV/LGP	0.73	0.0008	0.57	0.1109	0.20	0.4851	−0.05	0.8995
CPuRV/MGP	0.63	0.0067	0.45	0.2271	0.04	0.8848	−0.69	0.0583
CPuRD/LGP	0.83	<0.0001	0.35	0.3528	0.26	0.3679	−0.11	0.7910
CPuRD/MGP	0.79	0.0002	0.47	0.1987	0.04	0.8874	−0.53	0.1748
CPuC/LGP	0.72	0.0011	0.84	0.0044	0.18	0.5411	−0.81	0.0140
CPuC/MGP	0.51	0.0382	0.69	0.0395	0.11	0.7147	−0.39	0.3391

*r, Pearson correlation coefficients.

Table 4

PCA hMT1 and control mice

Component	Eigenvalue	Proportion of Variance	ROI #1	ROI #2	ROI #3	ROI #4	ROI #5	ROI #6	ROI #7
GU hMT1									
1	9.99	0.25	PAG (0.86)	S1HL (0.85)	IC (0.80)	Cg (0.76)			
2	8.97	0.22	Pn (0.86)	S1FL (0.84)	M1 (0.81)	SC (0.77)	SNR (0.72)		
3	6.52	0.16	S2 (0.93)	VM (0.79)	VL (0.73)	CPuRD (0.55)	IOM (0.51)		
4	5.69	0.14	SO (0.80)	DC (0.69)	SNC (0.63)	DLG (0.59)	LGP (0.57)		
5	3.54	0.09	RMC (0.83)	STh (0.83)	Med (0.66)	Aint (0.61)	Chem (0.58)		
Cumulative Variance		**0.87**							
CO hMT1									
1	18.33	0.36	IOD (0.93)	Pn (0.91)	VLG (0.85)	LSO (0.79)	IOM (0.72)	LD (0.71)	DLG (0.70)
2	8.90	0.17	RMC (0.95)	LGP (0.90)	PnO (0.83)	CPuC (0.81)	STh (0.76)	MG (0.72)	RMg (0.65)
3	7.28	0.14	CpuRD (0.76)	CpuRV (0.72)	MGP (0.69)	BLA (0.59)	S1FL (0.56)	LC (0.54)	S1HL (0.50)
4	5.38	0.11	Lat (0.91)	Aint (0.84)	DC (0.72)	Mve (0.70)	Med (0.53)		
5	5.05	0.10	ML (0.86)	PCL (0.82)	SNR (0.79)	S2 (0.54)	PAG (0.52)		
Cumulative Variance		**0.88**							
GU control									
1	10.73	0.27	M2 (0.84)	S2 (0.84)	S1BF (0.82)	Cg (0.74)			
2	5.37	0.13	IPC (0.79)	LC (0.73)	DLG (0.71)	Lat (0.59)	AInt (0.51)		
3	4.20	0.10	IOM (0.76)	Chem (0.74)	Cver (0.68)	IOD (0.67)	VL (0.52)		
4	3.93	0.10	RMg (0.73)	SO (0.71)	PnO (0.54)	VM (0.53)			
5	3.41	0.08	S1HL (0.86)	S1FL (0.81)					
Cumulative Variance		**0.69**							
CO control									
1	18.64	0.33	SO (0.92)	CA3poly (0.92)	SR (0.91)	Cg (0.89)	iDG (0.85)	H (0.84)	M2 (0.83)
2	7.73	0.14	S1HL (0.82)	S1FL (0.82)	S1BF (0.77)	S2 (0.74)	BLA (0.67)		
3	7.11	0.13	PCL (0.92)	ML (0.88)	GL (0.82)	LC (0.64)			
4	5.75	0.10	SuG (0.75)	DLG (0.75)	oDG (0.74)	PAG (0.61)	APTD (0.60)		

Component	Eigenvalue	Proportion of Variance	ROI #1	ROI #2	ROI #3	ROI #4	ROI #5	ROI #6	ROI #7
5	3.53	0.06	VL (0.70)	VM (0.65)	VA (0.61)				
Cumulative Variance		**0.76**							